Acta Materialia 200 (2020) 236–245

Contents lists available at ScienceDirect

Acta Materialia

journal homepage: www.elsevier.com/locate/actamat

Full length article

Highly deformable Mg–Al–Ca alloy with Al_2Ca precipitates

Gaoming Zhu[a,e], Leyun Wang[a,d,*], Jie Wang[a], Jian Wang[b], Jun-Sang Park[c], Xiaoqin Zeng[a,d]

[a] National Engineering Research Center of Light Alloy Net Forming, Shanghai Jiao Tong University, Shanghai, 200240, China
[b] Mechanical and Materials Engineering, University of Nebraska-Lincoln, Lincoln, NE, 68588, United States
[c] Advanced Photon Source, Argonne National Laboratory, Lemont, IL, 60439, United States
[d] State Key Laboratory of Metal Matrix Composites, Shanghai Jiao Tong University, Shanghai, 200240, China
[e] Department of Materials Science and Engineering, Massachusetts Institute of Technology, Cambridge, MA 02139, United States

ARTICLE INFO

Article history:
Received 24 June 2020
Revised 28 August 2020
Accepted 2 September 2020
Available online 8 September 2020

Keywords:
Magnesium alloys
Precipitation strengthening
Tension test
Synchrotron diffraction
Dislocations

ABSTRACT

Magnesium (Mg) is the lightest structural metal. However, the poor formability of Mg alloys to great extent limits their applications in making structural parts. Formability is strongly correlated to both high tensile elongation and large work hardening capacity. Here, we report a new Mg–Al–Ca alloy in which a majority of deformable Al_2Ca precipitates form while the formation of Laves phases of $Mg_{17}Al_{12}$ and Mg_2Ca seems suppressed. Al_2Ca precipitates impede dislocation motion, leading to large work hardening. Then, Al_2Ca precipitates deform with dislocations and stacking faults under the enhanced flow stress, which relieve local stress concentration and improve tensile elongation. In addition, solutes Al and Ca suppress twin nucleation while promoting $\langle c + a \rangle$ dislocations in Mg. This new Mg–Al–Ca alloy demonstrates one of the highest combinations of tensile elongation and work hardening capacity among existing Mg alloys.

1. Introduction

Magnesium (Mg) is the lightest structural metal. Commercial Mg alloys such as AZ31 possess higher specific strength than most aluminum alloys and steels [1]. Nonetheless, poor formability of Mg at room temperature limits the widespread applications of this metal [2]. Metal formability is generally correlated to tensile elongation and work hardening. Elongation measures the strain limit for a material to sustain uniaxial tension, while work hardening represents the material's resistance to necking [3]. Elongation of commercial Mg alloys (e.g., AZ31) is typically 10%–15% along the extrusion or rolling directions [4,5]. While the elongation of Mg can be improved by grain refinement [6–9], such efforts often reduce the work hardening.

Addition of rare earth (RE) elements such as Y, Ce, Gd, and Nd can enhance Mg's formability by both weakening the texture and activating non-basal slip [10–18]. When these alloys undergo proper heat treatment, fine Mg-RE precipitates can form on prismatic planes, which effectively inhibit basal dislocations and enhance strength as well [19]. WE series alloys (Mg–Y–Nd) with a combination of high strength and ductility are often used in aerospace applications [20]. Despite the advantages of Mg–RE alloys, the limited availability of rare earth makes it too expensive for general industries. Hence, RE-free Mg alloys are being searched continuously.

Ca, as a useful alloying element, has received more and more attention [21–23]. Recently, it has been found that a dilute co-addition of Al and Ca can enhance the elongation as well as the yield strength (YS) of Mg [24–26]. For example, a Mg–1.0Al–0.1Ca (wt.%) rolled alloy shows elongation of ~20% [24], which was attributed to the enhanced $\langle c + a \rangle$ activity. A Mg–0.6Al–0.28Ca–0.25Mn (wt%) extruded alloy exhibits YS of 253 MPa at the peak-aged T6 condition because of the formation of Al–Ca-rich Guinier-Preston (G.P.) zones, which provides resistance against dislocation motion [26]. In all those studies, Al and Ca were kept below their solubility limits to prevent the formation of Laves phases of $Mg_{17}Al_{12}$ (A12, cubic structure) and Mg_2Ca (C14, hexagonal structure), which are generally detrimental for the material's ductility.

Herein, we report the development of a new Mg–6Al–1Ca (wt%) alloy that possesses both high elongation and strong work hardening. By carefully controlling the alloy chemistry and processing procedures, the formation of $Mg_{17}Al_{12}$ and Mg_2Ca were avoided. Instead, precipitation of Al_2Ca was found in its microstructure. Those Al_2Ca precipitates are nonshearable but deformable. As a result, this Mg–Al–Ca alloy demonstrates one of

* Corresponding author.
E-mail addresses: leyunwang@sjtu.edu.cn, wly857@gmail.com (L. Wang).

https://doi.org/10.1016/j.actamat.2020.09.006
1359-6454/

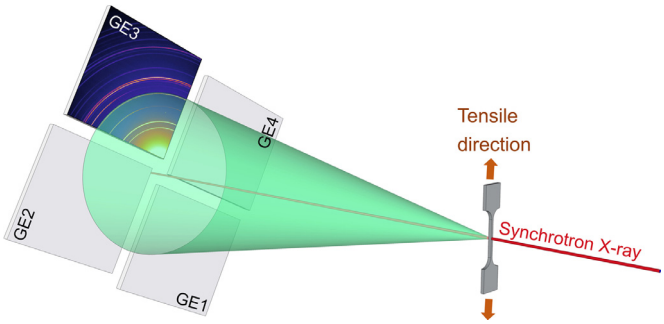

Fig. 1. A schematic of the in situ tensile test with synchrotron X-ray diffraction.

the highest combinations of tensile elongation and work hardening capacity among existing Mg alloys. With its simple composition, this new Mg alloy will be very attractive for industrial applications.

2. Experimental procedures

Commercial-purity Mg (99.95%), Al (99.95%), and a Mg–20 wt% Ca master alloy were used to prepare the Mg–6Al–1Ca (wt%) alloy. The raw materials were melted in an electric resistance furnace at 750 °C under a protective atmosphere of CO_2 (99 vol.%) and SF_6 (1 vol.%) gas mixture. After refining, the melted liquid was cooled to 730 °C and then cast into an ingot (Φ60 mm × 120 mm). The ingot was solution treated at 450 °C for 24 h, followed by extrusion at 250 °C with extrusion ratio = 18:1 and extrusion speed = 2 mm s^{-1}. Calculation of phase fractions was performed using the Thermo-Calc™ 2020a software in conjunction with the database TCMG5 (version 5.1). The calculation range is 0 to 700 °C, with an interval of 1 °C.

In situ synchrotron X-ray diffraction experiment was performed at the beamline 1–ID of the Advanced Photon Source (APS) at Argonne National Laboratory. The X-ray energy was 71.68 keV (wavelength λ = 0.1730 Å), and the size of the beam was 150 μm × 150 μm. Fig. 1 shows the schematic of the in situ experiment, four area detectors (GE1, GE2, GE3, and GE4) were placed approximately 2.6 m away from the specimen to collect the diffraction data. Detector geometric parameters such as the detector distance, detector tilt angles, and the beam center were calibrated using a CeO_2 standard sample by checking the radii and the eccentricity of the diffraction rings. A flat dog-bone shaped tensile specimen with a gage length of 5 mm and a cross-section of 1.0 × 1.0 mm^2 had been extracted from the Mg–6Al–1Ca extruded bar, with the tensile axis being parallel to the extrusion direction. During the tensile test, the crosshead speed on the specimen was constant at 0.03 mm min^{-1}, equivalent to a nominal strain rate of 1.0 × 10^{-4} s^{-1}. The detectors recorded the diffraction patterns at 20 s to 65 s intervals during the tensile test. Diffraction patterns from the GE3 detector were used to analyze the lattice strain of different peaks; diffraction patterns from both GE2 and GE3 detectors were used to analyze the full width at half maximum (FWHM) of different peaks.

The two-dimensional diffraction rings were integrated along the azimuthal directions to one-dimensional diffraction profiles. Each diffraction peak was fitted by a Gaussian function to extract its peak position and FWHM. The d-spacing of the corresponding {*h k l*} plane, $\boldsymbol{d}_{hkl}$, was calculated by the Bragg's law:

$$d_{hkl} = \frac{\lambda}{2sin\theta_{hkl}} \quad (1)$$

where λ = 0.1730 Å is the X-ray wavelength and θ_{hkl} is the diffraction angle. Lattice strain, ε_{hkl} is calculated as:

$$\varepsilon_{hkl} = \frac{d^1_{hkl} - d^0_{hkl}}{d^0_{hkl}} \quad (2)$$

where d^0_{hkl} and d^1_{hkl} are the d-spacing of the {*h k l*} plane before deformation and under certain strain, respectively.

Transmission electron microscopy (TEM) was employed to characterize the Al_2Ca precipitates and the surrounding dislocation configuration microstructure using a JEOL JEM–2100F instrument. TEM samples were twin-jet electropolished in a solution of ethanol – 4% perchloric acid electrolyte at 30 V and −40 °C, followed by ion milling. Burgers vectors of the observed dislocations were analyzed by the invisibility criterion $\boldsymbol{g}\cdot\boldsymbol{b} = 0$. ⟨a⟩ type dislocations are visible under the $\boldsymbol{g} = (10\bar{1}0)$ condition but invisible under the $\boldsymbol{g} = (0002)$ condition; ⟨*c* + *a*⟩ type dislocations are visible under both the $\boldsymbol{g} = (10\bar{1}0)$ and $\boldsymbol{g} = (0002)$ conditions. Using the TEM samples, transmission Kikuchi diffraction (TKD) was performed using a GAIA3 instrument (Tescan, Czech Republic).

Slip trace analysis was also performed to statistically examine the slip activity in the Mg phase. A flat dog-bone shaped tensile specimen with a gage dimension of 11 mm (length) × 4.0 mm (width) × 1.4 mm (thickness) was mounted in a MICROTEST 200 N (Deben, UK) module placed in a Zeiss Gemini scanning electron microscope (SEM) with an electron backscatter diffraction (EBSD) system (Oxford Instrument, UK). The tension direction was also parallel to the extrusion direction. The top surface of the specimen had been mechanically ground and electro-polished in ethanol – 10% perchloric acid electrolyte at 30 V for 150 s at −30 °C for EBSD characterization. After the initial EBSD scan, the specimen was loaded at a crosshead speed of 0.1 mm min^{-1}, equivalent to a nominal strain rate of 1.5 × 10^{-4} s^{-1}. The test was paused at different strains for secondary electron imaging and more EBSD scans of the same surface region. Slip trace analysis was performed for the observed slip lines. A set of parallel slip lines in a given grain is associated with dislocation glide on a particular slip plane. These slip lines should be parallel to the intersection line between the slip plane and the sample surface. Based on the grain orientation measured by EBSD, we computed the directions of all possible slip planes in the sample coordinate system and drew their intersections with the surface plane. Comparing the computational result with the observed slip lines allowed us to infer the activated slip system. More details of slip trace analysis can be found in [27].

3. Results

3.1. Mg–Al–Ca alloy development and microstructure characterization

A Mg–6Al–1Ca (wt%) alloy (AX61) was obtained by the above homogenization-extrusion procedure. Fig. 2(a) shows our thermodynamics calculation of the phase fractions as a function of temperature for this composition using the Thermo-Calc™ software. After casting, the alloy was homogenized at 450 °C for 24 h and then extruded at 250 °C, as demonstrated in Fig. 2(b). The chosen thermomechanical path prevented the formation of eutectic A12 $Mg_{17}Al_{12}$ and C36 $(Mg, Al)_2Ca$ (dihexagonal structure) [26]. Instead, C15 Al_2Ca (cubic structure) was the only type of precipitate found in the material, as revealed by synchrotron X-ray diffraction (Fig. 3(a, b)).

Fig. 3(a) shows the initial diffraction pattern of the AX61 tensile specimen from the GE3 detector. After integrating the diffraction pattern along the azimuthal direction (Fig. 3(b)), all diffraction peaks were identified either from Mg or Al_2Ca. From the diffraction profile, the volume fraction of Al_2Ca is estimated to be 4.2% using

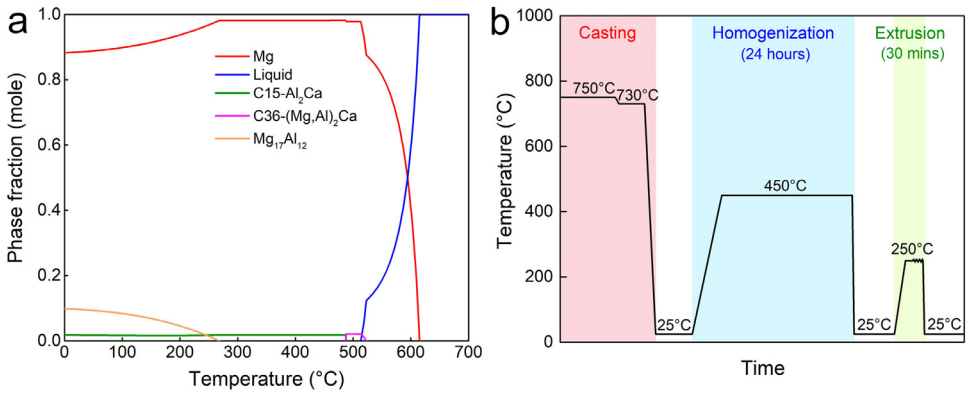

Fig. 2. Alloy development. (a) Calculated phase fractions as a function of temperature for the Mg–6Al–1Ca (wt%) composition. (b) The thermomechanical processing path of the alloy.

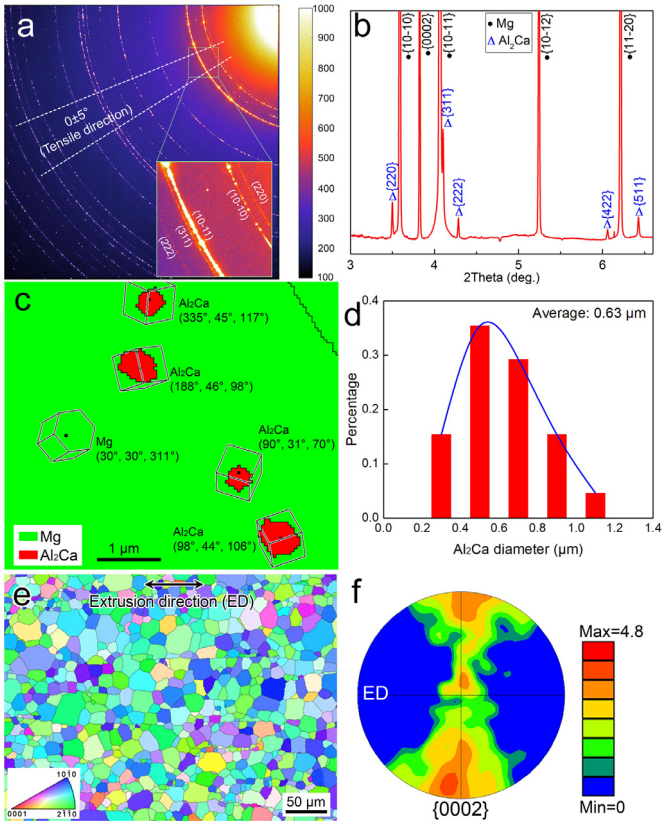

Fig. 3. Microstructure characterization of the AX61 alloy. (a) Synchrotron X-ray diffraction pattern of the AX61 alloy. (b) The resultant diffraction profile by integrating the diffraction pattern along the azimuthal direction over a range of 90°. (c) Phase mapping by TKD to show Al_2Ca precipitates in a Mg grain. Orientations of Al_2Ca and the Mg grain are represented by unit cells and Euler angles. (d) Size distribution of the Al_2Ca precipitates characterized by TKD. (e, f) Inverse pole figure (IPF) map and {0002} pole figure of the Mg phase by EBSD.

the MAUD software [28]. Transmission Kikuchi diffraction (TKD) was further taken to analyze a total of 29 Al_2Ca precipitates from 15 Mg grains. Unlike many other precipitates with a definite orientation relationship (OR) with respect to the surrounding Mg, those Al_2Ca are nearly random-oriented (Fig. 3(c)). The Al_2Ca precipitates are equiaxed with an average diameter of 0.63 μm (Fig. 3(d)). The Mg phase exhibits a fully recrystallized microstructure with an average grain size of ~19 μm, as shown by the EBSD scan result in Fig. 3(e). The associated {0002} pole figure (Fig. 3(f)) indicates that the alloy has a moderate extrusion fiber texture (m.r.d. = 4.8). Due to the relatively large step size (1 μm) for this EBSD scan, no Al_2Ca phase was indexed.

3.2. Tensile properties of the AX61 alloy

Fig. 4(a) shows the stress-strain curve of the AX61 alloy from the in situ tensile test at beamline 1-ID of APS. The experimental setup is illustrated in Fig. 1. While the specimen displays a moderate yield strength (YS) of 125 MPa, it shows tensile elongation of 27% and ultimate tensile strength (UTS) of 260 MPa. The difference between UTS and YS can be taken as a measure of work hardening capacity. Fig. 4(b) and Table 1 compare the tensile elongation and the UTS−YS values of different Mg wrought alloys. The AX61 alloy is located at the upper-right corner, indicating it has better formability than almost all other alloys. The only comparable alloy is Mg−1Mn−1Nd (wt%, MN11). The MN11 alloy has a slightly smaller grain size (~15 μm) than AX61 (~19 μm), but its strength (YS = 105 MPa, UTS = 240 MPa) is lower than AX61 (YS = 125 MPa, UTS = 260 MPa). Besides, the MN11 alloy contains an expensive rare earth element of Nd. Therefore, the AX61 alloy is overall superior to MN11.

3.3. Deformation mechanisms in AX61

Debye rings of the Mg $\{11\bar{2}0\}$ peak around the tensile direction at the strains of 0% and 25% are shown in Fig. 5(a). The discrete diffraction spots at 0% strain became connected due to the accumulated dislocations after 25% strain. The Debye rings were integrated into one-dimensional profiles over a range of ±5° around the tensile direction, which is called the axial diffraction profile. Fig. 5(b) shows the Mg $\{11\bar{2}0\}$ peak from the axial diffraction profile. The peak position shifted towards smaller 2-θ values, indicating an increase of the d-spacing of the Mg $\{11\bar{2}0\}$ plane.

Lattice strains associated with the Mg $\{11\bar{2}0\}$ peak and other peaks can be computed from the peak shifting using Eq. (2). Fig. 5(c, d) show the evolution of lattice strains of different Mg and Al_2Ca peaks as a function of the macroscopic strain. For the Mg phase, its $\{10\bar{1}1\}$, $\{10\bar{1}2\}$, $\{10\bar{1}3\}$ peaks exhibited lower lattice strains than $\{10\bar{1}0\}$ and $\{11\bar{2}0\}$, indicating that basal slip is easier than prismatic slip to be activated in this material [42]. For the Al_2Ca phase, lattice strains of its {222}, {422}, {511}, and {440} peaks are slightly higher than the Mg $\{10\bar{1}0\}$ and $\{11\bar{2}0\}$ peaks. The Young's modulus of Al_2Ca is approximately 103 GPa [45], which is more than twice that of Mg (45 GPa). Therefore, the Al_2Ca phase bears more stress than the Mg phase. To further analyze the stress partitioning between Mg and Al_2Ca, lattice strains of different peaks in both phases were plotted as a function of the applied stress in Fig. 5(e, f). In the elastic deformation stage,

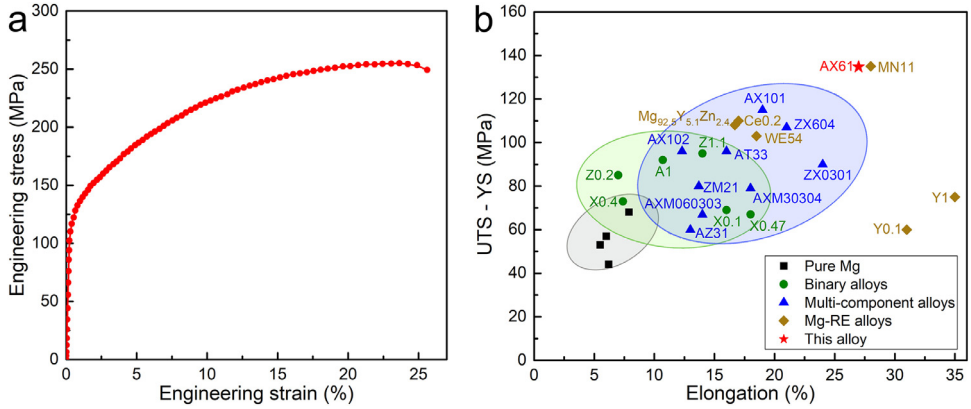

Fig. 4. Tensile properties of the AX61 alloy. (a) Engineering stress-strain curve of the AX61 alloy. (b) Comparison of the elongation and UTS−YS values of different Mg wrought alloys. Detailed data are listed in Table 1.

Table 1
Tensile properties and grain size of different Mg wrought alloys.

Composition (wt.%)	Processing path	Grain size (μm)	UTS (MPa)	YS (MPa)	Elongation	Ref.
Mg	Extrusion	25	130	73	0.06	[29]
Mg	Extrusion + annealing	21	169	125	0.062	[30]
Mg	Rolling + annealing	14	185*	132	0.055	[9]
Mg	Extrusion	19	153	85	0.079	[31]
Mg-0.99Al	Extrusion + annealing	40	248	156	0.107	[32]
Mg-0.1Ca	Rolling + annealing	45	168	99	0.16	[33]
Mg-0.4Ca	Rolling + annealing	57	175	102	0.074	[33]
Mg-0.47Ca	Extrusion	35	162	95	0.18	[27]
Mg-0.2Zn	Rolling + annealing	22	170*	85	0.07	[34]
Mg-1.1Zn	Rolling+ annealing	25	195*	100	0.14	[34]
Mg-3Al-1Zn	Extrusion	13	275*	215	0.13	[35]
Mg-3Al-3Sn	Rolling + annealing	41	223	127	0.16	[36]
Mg-0.3Zn-0.1Ca	Rolling + annealing	58	182	92	0.24	[33]
Mg-6Zn-0.36Ca	Extrusion	14	276	169	0.21	[37]
Mg-1.9Zn-1.0Mn	Extrusion	18	251	171	0.137	[38]
Mg-1.1Al-0.24Ca	Extrusion + annealing	29	191	95	0.123	[39]
Mg-1Al-0.1Ca	Rolling + annealing	35	220	105	0.19	[24]
Mg-2.73Al-0.34Ca-0.44Mn	Extrusion + annealing	13	267	188	0.18	[25]
Mg-0.6Al-0.28Ca-0.25Mn	Extrusion	27	232	165	0.14	[26]
Mg-0.2Ce	Rolling + annealing	25	220*	110	0.17	[40]
Mg-0.1Y	Extrusion + annealing	23	190	130	0.31	[41]
Mg-1Y	Extrusion + annealing	21	180	105	0.35	[41]
Mg-5.1Y-2.4Zn	Extrusion	10	285	177	0.167	[42]
Mg-1Mn-1Nd	Extrusion	15	240	105	0.28	[43]
Mg-5Y-1.6Nd-2.6RE	Extrusion	17	273*	170	0.185	[44]
Mg-6Al-1Ca	Extrusion	19	260	125	0.27	This work

* We converted the true stress-strain curves to engineering stress-strain curves to obtain those UTS values.

lattice strains in both phases increased linearly with the applied stress. At about 125 MPa, lattice strains of Mg $\{10\bar{1}2\}$ and $\{10\bar{1}3\}$ peaks decreased while lattice strains of all Al_2Ca peaks increased substantially, indicating load transfer from the Mg matrix to Al_2Ca precipitates.

Deformation also broadened the peaks (see Fig. 5(b)). To quantify peak broadening, the patterns should not be integrated over a large azimuthal range of 90°, as the deviation in lattice strain along different sample directions will cause artifacts in the computed FWHM [46–48]. Instead, the two-dimensional diffraction pattern was caked into 10° azimuthal slices from the axial direction (0°) to the transverse direction (90°). Each slice was then integrated into individual 1D profiles. Those profiles were fit with Gaussian functions to obtain the FWHM and integrated intensity of each peak of interest. The FWHM results were averaged over all measured azimuthal slices using integrated intensity weighting. Fig. 5(g) shows that the FWHMs of Mg peaks increased moderately with strain as the result of dislocation accumulation. In contrast, FWHMs of Al_2Ca peaks increased much more rapidly with strain (Fig. 5(h)), indicating ultrahigh microstrains in Al_2Ca precipitates. Similar behaviors were previously observed in an age-hardened Mg−2.2wt%Nd alloy with abundant Mg_3Nd precipitates [49]. In that alloy, the Mg_3Nd precipitates can be sheared by basal dislocations, which causes the large internal microstrain.

Deformation in the Mg phase was further studied by surface slip trace analysis. Fig. 6(a, b) shows the IPF map and corresponding SEM image of a small area from the specimen used in the in situ SEM/EBSD test after 4% strain. Deformation twins are rarely observed, so almost all grains were deformed by slip. From the slip trace analysis, basal slip is the dominant deformation mode, while prismatic, pyramidal I, and pyramidal II slip lines were also occasionally found. Slip trace analysis was then performed in a larger area with 176 grains. At 4% strain, about 80% of the observed slip traces belong to basal slip. Most non-basal slip traces initiated from grain boundaries (Fig. 7). Notably, pyramidal II slip traces, which are associated with $\langle c + a \rangle$ dislocations were observed in AX61 at this early deformation stage. In contrast, our previous study of as-extruded Mg−0.47wt%Ca and AZ31 alloys showed no pyramidal II slip traces at 4% strain [27]. Those $\langle c + a \rangle$ dislocations are critical for the high formability of the AX61 alloy.

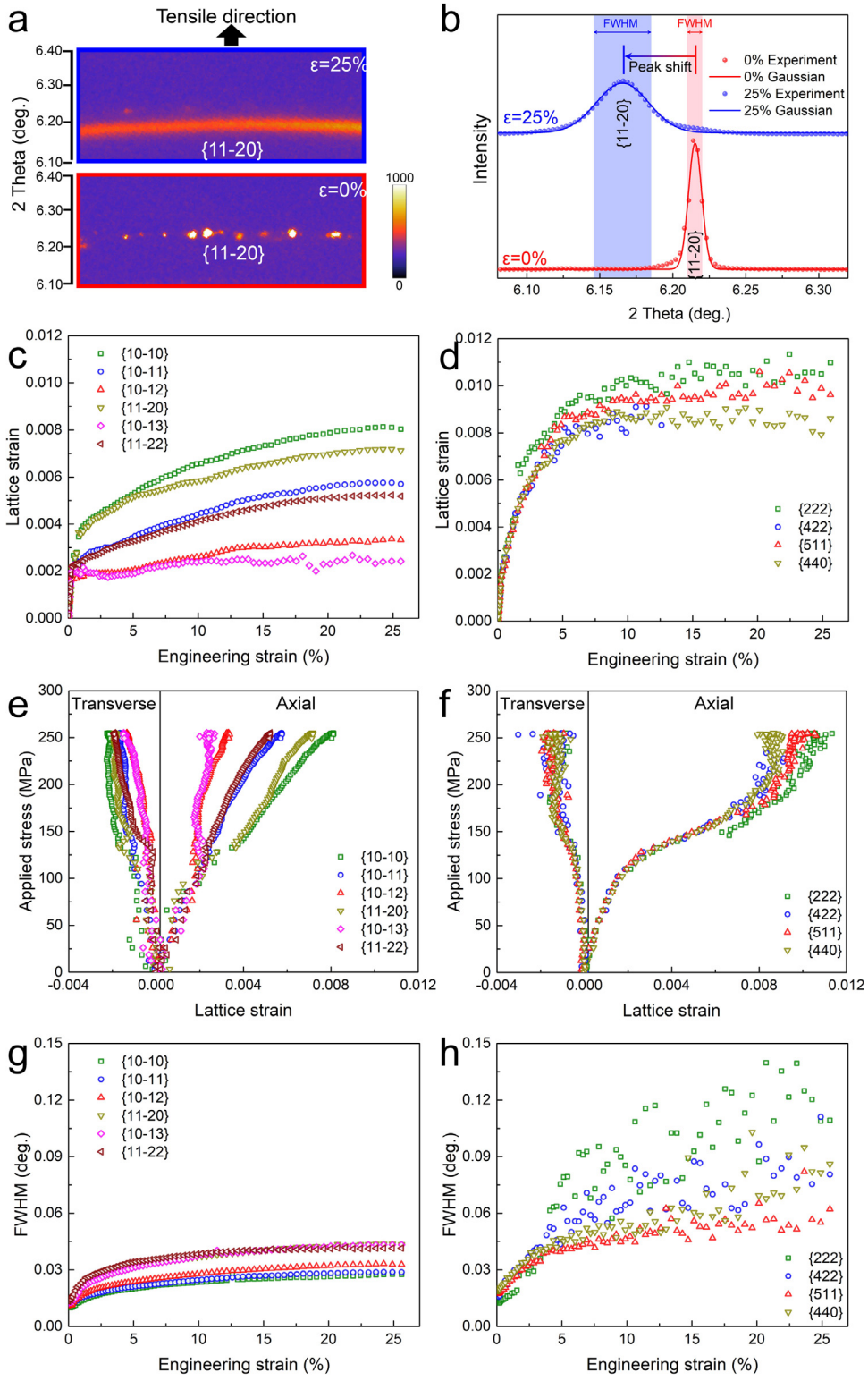

Fig. 5. Analysis of the diffraction peaks of Mg and Al_2Ca. (a) Debye rings of the Mg $\{11\bar{2}0\}$ peak near the tensile direction at strains of 0% and 25%. (b) Integrated diffraction profiles around the tensile direction over a range of ±5° near the Mg $\{11\bar{2}0\}$ peak. (c, d) Lattice strain evolution of different peaks in Mg and Al_2Ca along the tensile (axial) direction. (e, f) Lattice strain as a function of the applied stress of different peaks in Mg and Al_2Ca along both the axial and the transverse directions. (g, h) FWHM evolution of Mg and Al_2Ca peaks.

TEM analysis was performed to characterize the deformation of Al_2Ca precipitates. Unlike Mg_3Nd, we did not observe any Al_2Ca precipitate being sheared by dislocations. Instead, dislocations and {111} stacking faults were observed in many Al_2Ca precipitates after only 2% and 4% strain, as shown in Fig. 8(a, b). Those dislocations and stacking faults developed inside Al_2Ca precipitates would induce heterogeneous microstrain and cause diffraction peak broadening (see Fig. 5(h)), especially for the {222} peak.

Since Al_2Ca precipitates do not hold a certain orientation relation with the Mg matrix, slip transmission for dislocations from

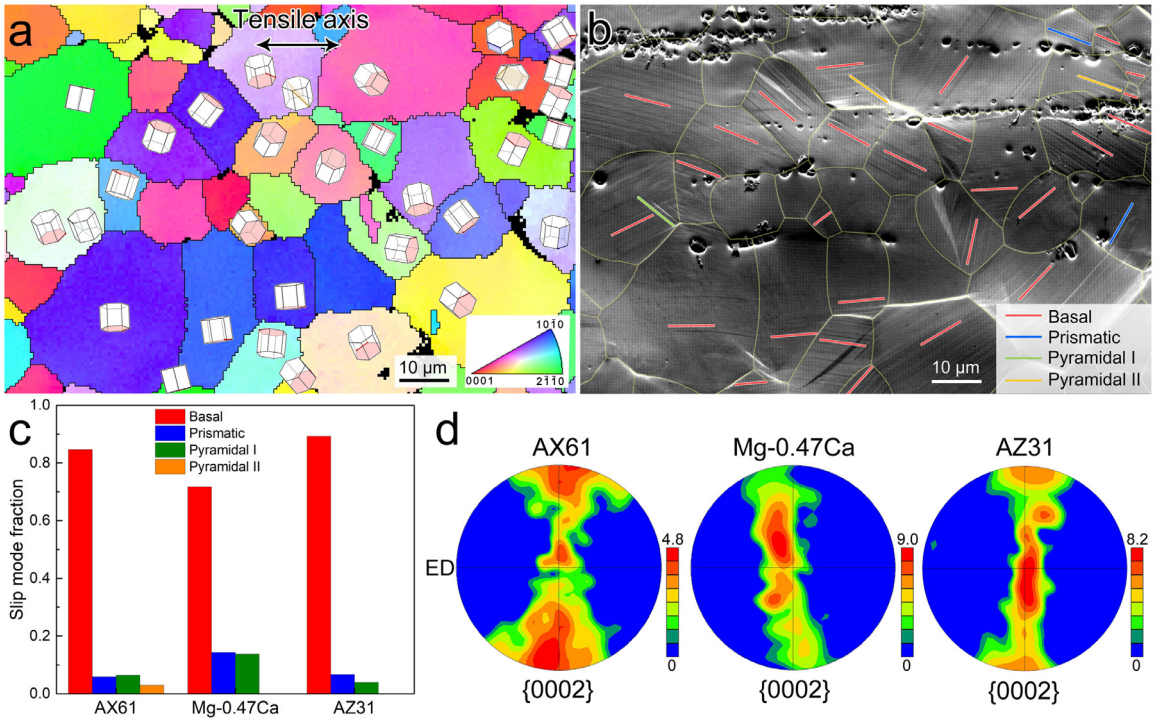

Fig. 6. Surface slip trace analysis. (a) Grain orientations from a small region by EBSD measurement. (b) The slip traces observed at 4% strain were marked according to the identified slip systems. (c) Statistics of the identified slip activity in AX61, Mg–0.47 wt% Ca, and AZ31 at 4% strain. (d) {0002} pole figures of the three extruded alloys.

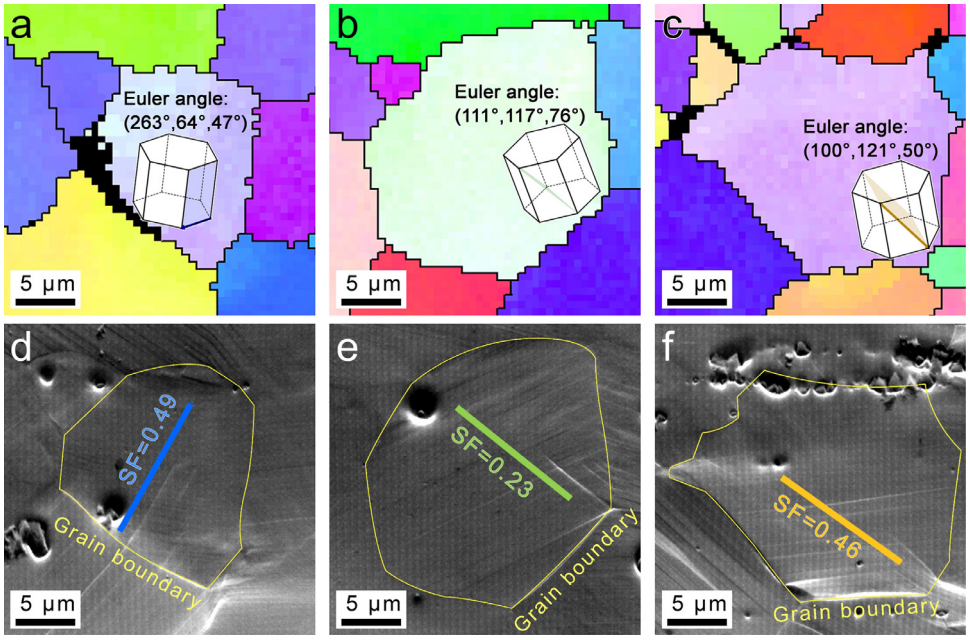

Fig. 7. Non-basal slip traces often initiated from grain boundaries: (a, d) prismatic slip, (b, e) pyramidal I slip, and (c, f) pyramidal II slip.

matrix into precipitates would be difficult. It is expected that the so-called geometrically necessary dislocations (GNDs) would form around those Al_2Ca precipitates [50]. This hypothesis was actually confirmed by TEM observations. An example is shown in Fig. 9. Dislocations visible at the $\boldsymbol{g} = (10\bar{1}0)$ condition are $\langle a \rangle$ dislocations on the basal plane, while dislocations visible at the $\boldsymbol{g} = (0002)$ condition are $\langle c + a \rangle$ dislocations. Three $\langle c + a \rangle$ dislocations apparently nucleated from the lower-left Al_2Ca precipitate into the adjacent Mg matrix. Those $\langle c + a \rangle$ dislocations likely formed to accommodate stress concentration near the Mg/Al_2Ca interface.

4. Discussion

Here, we compare the tensile properties of the AX61 alloy (YS = 125 MPa, UTS = 260 MPa, elongation = 27%) with a conventional AZ31 alloy [51] (YS = 173 MPa, UTS = 238 MPa, elongation = 12%). The two extruded alloys are similar in grain size (19 μm vs 21 μm) and texture strength (4.8 m.r.d vs 3.8 m.r.d), so the difference in their tensile properties must be attributed to the deformation mechanisms. YS of AX61 is lower than that of AZ31 by about 48 MPa. From Fig. 6(c), basal slip dominates the early

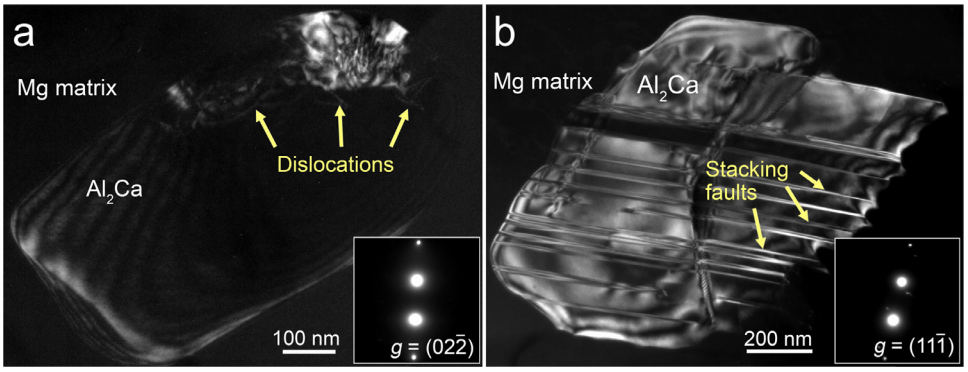

Fig. 8. Deformation of Al_2Ca by TEM observation. (a) Two-beam dark-field (TBDF) image of an Al_2Ca precipitate at 2% strain, taken along the [011] zone axis under $\boldsymbol{g} = (02\bar{2})$ condition, which shows dislocations inside this Al_2Ca precipitate. (b) TBDF image of another Al_2Ca precipitate at 4% strain, taken along the [011] zone axis under $\boldsymbol{g} = (11\bar{1})$, which shows stacking faults inside this Al_2Ca precipitate.

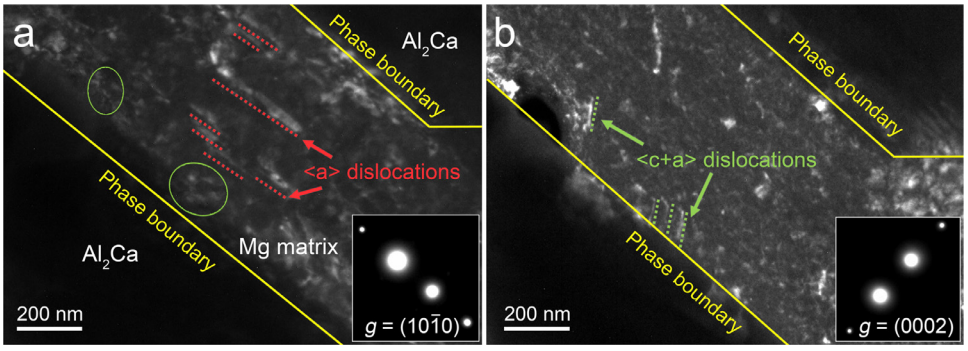

Fig. 9. Dislocation analysis near an Al_2Ca /Mg boundary. (a) TBDF image taken along the [1$\bar{2}$10] zone axis under $\boldsymbol{g} = (10\bar{1}0)$ condition. (b) TBDF image taken along the [1$\bar{2}$10] zone axis under $\boldsymbol{g} = (0002)$ condition.

deformation stages in both AX61 and AZ31. Therefore, the YS of AX61 being lower must be attributed to the softening of basal slip, which is likely caused by solute Ca in relative to solute Zn. Cihova et al. [26] showed that in a peak-aged Mg–0.6Al–0.28Ca–0.25Mn (wt%) extruded alloy, YS can be as high as 236 MPa. In that alloy, ordered monolayer G.P. zones with Al:Ca=2 and average plate diameter of 3.6 nm were formed on the basal plane. The G.P. zones had a high number density to effectively block basal dislocations; it was estimated that the G.P. zones increase the YS by 66 MPa. In the present AX61 alloy, the Al_2Ca precipitates have an average diameter of 0.63 μm, which is two orders of magnitude larger than the G.P. zones. Thus, the initial strengthening effect of Al_2Ca should be very limited.

After yielding, however, the AX61 alloy displayed strong work hardening and high elongation. Work hardening generally arises from the increase of dislocation density, ρ. According to the Kocks-Mecking theory [52], the dislocation density evolution in the plastic deformation stage can be described by the following equation:

$$\frac{\partial \rho}{\partial \varepsilon^P} = k_1 \rho^{\frac{1}{2}} - k_2 \rho + k_D \tag{3}$$

where ε^P is the plastic strain, k_1, k_2 and k_D are constants. On the right hand side of Eq. (3), the first term represents the statistical storage of dislocations. The second term is the dynamic recovery term, which depends on strain rate and solute concentration. The third term is related to the geometrically necessary dislocations (GNDs) formed around nonshearable precipitates [53]. Since Al_2Ca is nonshearable, the $\langle c + a \rangle$ dislocations in Fig. 9 are essentially GNDs. Nucleation of GNDs around Al_2Ca increases the total dislocation density and cause the strong work hardening in the AX61 alloy. On the other hand, because Al_2Ca precipitates are internally deformable, stress concentration at the Mg/Al_2Ca interface can be quickly relieved, so the material can maintain high ductility.

The plastic deformation of Al_2Ca is also worth discussion. Al_2Ca has the C15 cubic structure. The atomistic coordinates of Al and Ca are 8a (0.125, 0.125, 0.125) and 16d (0.50, 0.50, 0.50), respectively, making the C15 structure similar to the FCC structure. The lattice constant of Al_2Ca is 0.801 nm [54]. The Burgers vector length of the {111}<110> slip system is about 0.57 nm in Al_2Ca, which is comparable to the Burgers vector length of $\langle c + a \rangle$ dislocations (~0.61 nm) in Mg.

High tensile elongation is usually achieved in those Mg alloys with rare earth solutes [8,10,11,13,15,16]. Rare earth solutes can randomize the extrusion/rolling texture, suppress twin nucleation, and make non-basal slip more active, all of which are beneficial for material ductility. From Fig. 6(d), this AX61 alloy displays a moderate extrusion texture. In situ EBSD was conducted for the AX61 alloy at 0, 1%, 2%, 4%, 8%, and 16% strains (Fig. 10). Twin volume fractions at different strains were measured and summarized in Fig. 11. After 16% strain, only 1.5% of the volume became twins. For comparison, the Mg–0.47Ca alloy previously studied in [27] developed more twins. Therefore, deformation twining is suppressed in AX61.

Finally, pyramidal $\langle c + a \rangle$ slip lines were found in this AX61 alloy (Fig. 6(c)). In pure Mg, $\langle c + a \rangle$ dislocations are difficult to glide because of the pyramidal-to-basal transition [55]. Rare earth solutes, such as Y, can make $\langle c + a \rangle$ dislocations glissile by accelerating cross-slip of $\langle c + a \rangle$ dislocations between pyramidal I and II planes [15]. Through first-principles computations, Ahmad et al. [56] recently found that 2 at% Al and 0.06 at% Ca solutes together can potentially promote the above cross-slip of $\langle c + a \rangle$ dislocations. That theory can account for the enhanced $\langle c + a \rangle$ slip in this AX61 alloy. By accommodating c-axis plastic deformation and

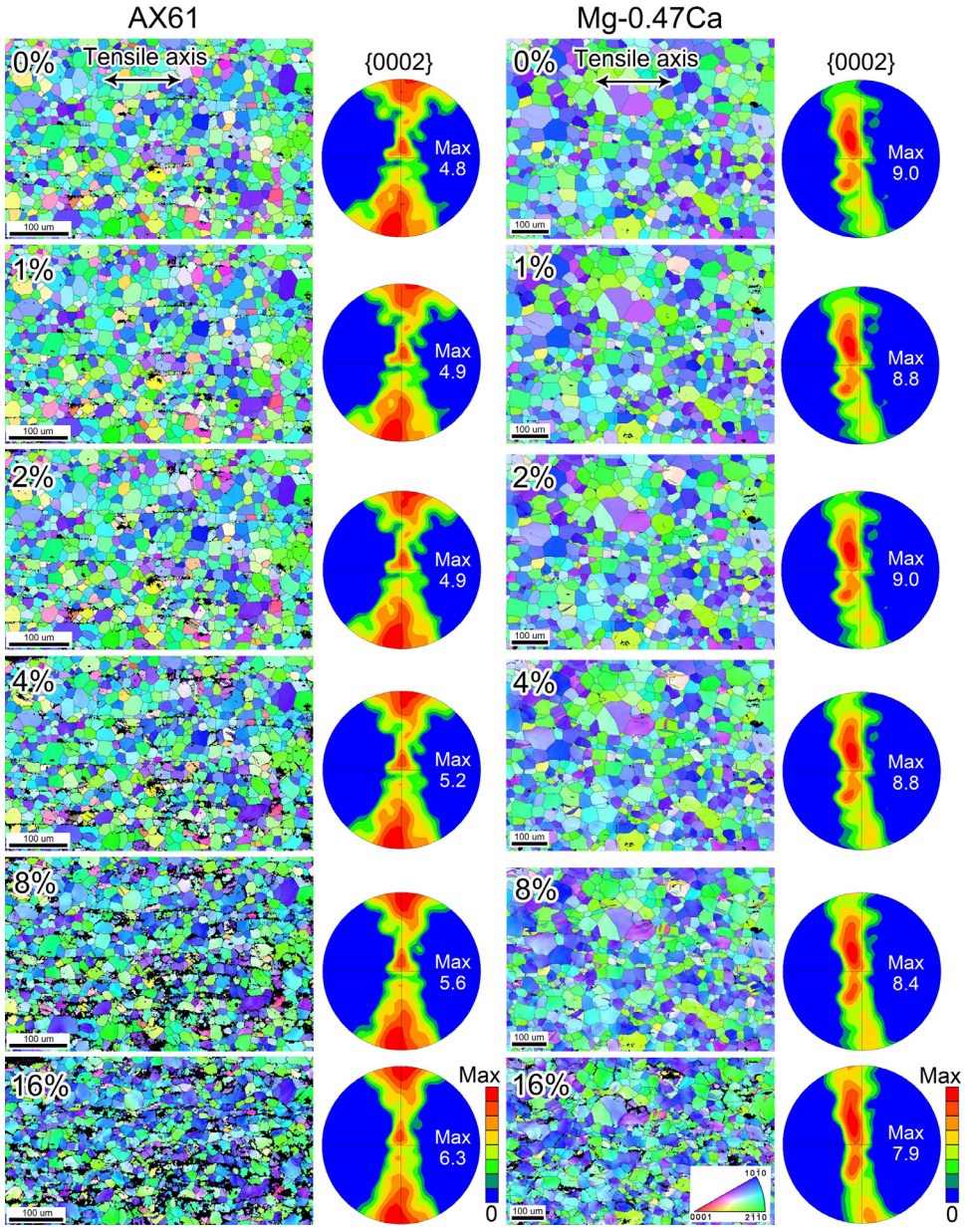

Fig. 10. Inverse pole figure maps and {0002} pole figures at different tensile strains for AX61 and Mg-0.47Ca.

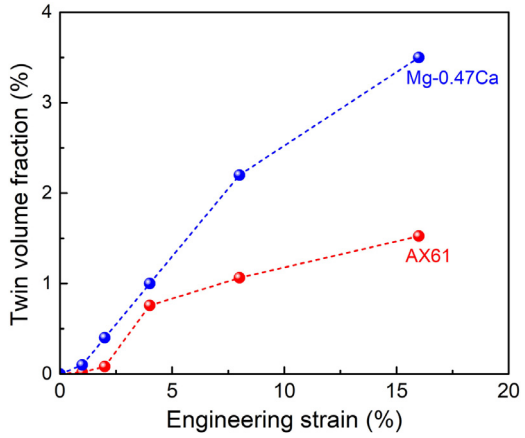

Fig. 11. Twin volume fractions at different tensile strains for AX61 and Mg–0.47Ca.

alleviate stress concentration at grain boundaries, the activation of $\langle c + a \rangle$ slip often improves the tensile elongation of Mg [13,24]. Using micromechanical tests, Liu et al. [57,58] demonstrated that the glide of $\langle c + a \rangle$ dislocations significantly increases the flow stress in Mg during deformation, which may be another reason for the large work hardening in the AX61 alloy.

A few experimental studies using atom probe tomography (APT) [21,59] and high-angle annular dark-field scanning transmission electron microscopy (HAADF-STEM) [60] show that Ca, like some rare earth elements, tend to segregate at grain boundaries and twin boundaries. First-principle calculations also suggest that Ca has one of the largest grain boundary/twin boundary segregation energy [61]. Somekawa et al. [62] recently observed that non-basal dislocations often nucleate from grain boundaries in Mg–Y and Mg–Ca, and they proposed that the grain boundary segregation of Y and Ca can activate non-basal dislocations. In the present AX61 alloy, grain boundaries are the primary nucleation sites of non-basal slip. In fact, 75% of the prismatic slip traces, 85% of the pyra-

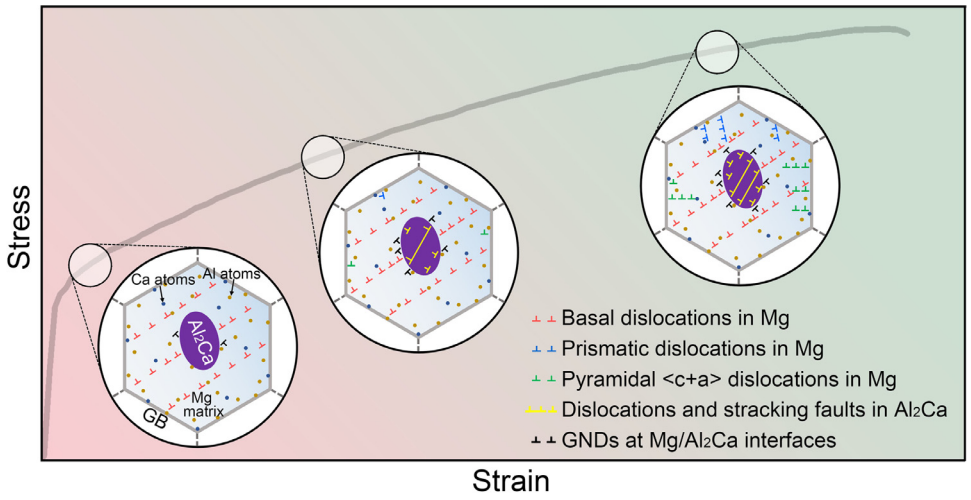

Fig. 12. Schematic of the deformation mechanisms in the AX61 alloy.

midal I slip traces, and 100% of the pyramidal II slip traces initiated from grain boundaries. Those non-basal slip may be caused by grain boundary segregation of Ca.

A schematic of the deformation mechanisms in AX61 is shown in Fig. 12. Upon yielding, basal slip was first activated in Mg. Dislocation pile-up at the Al_2Ca/Mg interfaces generates GNDs. Al_2Ca deformed subsequently by dislocation slip or stacking faults on the {111} plane. Non-basal dislocations are generated from grain boundaries due to the segregation of Ca. The nonshearable but deformable Al_2Ca, along with the enhanced $\langle c + a \rangle$ dislocation activity are responsible for the large work hardening and high tensile elongation of this material.

5. Conclusions

In this work, we designed an extruded Mg–6Al–1Ca (wt%) alloy, AX61. This alloy displays one of the highest combinations of tensile elongation (~27%) and work hardening (UTS – YS = 135 MPa). In situ synchrotron X-ray diffraction and electron microscopy were employed to study the deformation of this alloy. The main conclusions are summarized as follows:

(1) The AX61 alloy shows a moderate extrusion texture and a fully recrystallized microstructure with a mean grain size of ~19 μm. The alloy contains Al_2Ca precipitates with a volume fraction of ~4.2% and average diameter of 0.63 μm.
(2) During deformation, basal slip is the main deformation mode while twining is suppressed in the Mg phase. Non-basal slips, especially pyramidal II $\langle c + a \rangle$ slip can be activated from grain boundaries at the early deformation stage. The activation of non-basal slip systems, which is attributed to solute Al and Ca, enhances the ductility of this alloy.
(3) The Al_2Ca precipitates are nonshearable by dislocations in Mg, but they can deform plastically by forming internal dislocations and stacking faults. Stress concentration at the Mg/Al_2Ca interface can be quickly relieved by the internal plasticity of Al_2Ca, so the material can maintain high ductility.
(4) Nucleation of geometrically necessary dislocations (GNDs) around Al_2Ca increases the total dislocation density, and it leads to the strong work hardening of this alloy.

Declaration of Competing Interest

The authors declare that they have no known competing financial interests or personal relationships that could have appeared to influence the work reported in this paper.

Acknowledgements

We acknowledge J.H. Wang and P.P Jin (Qinghai University) for assistance in SEM/EBSD experiments. This work has been financially supported by the National Key Research and Development Program of China (No. 2016YFB0701203) and the National Natural Science Foundation of China (Nos. 51631006, 51671127, 51825101). L.W. is sponsored by the Youth Cheung Kong Scholars Program and the Shanghai Rising-Star Program. Use of the Advanced Photon Source was supported by the United States Department of Energy, Office of Science, Office of Basic Energy Sciences, under Contract No. DE-AC02–06CH11357.

References

[1] T.M. Pollock, Weight loss with magnesium alloys, Science 328 (2010) 986–987.
[2] B.C. Suh, M.S. Shim, K.S. Shin, N.J. Kim, Current issues in magnesium sheet alloys: where do we go from here? Scripta Mater. 84–85 (2014) 1–6.
[3] M.T. Pérez-Prado, J. Bohlen, S. Yi, D. Letzig, T. Al-Samman, J. Robson, M. Barnett, W. Poole, C. Mendis, S. Agnew, N. Stanford, Emerging hot topics and research questions in wrought magnesium alloy development, JOM 72 (2020) 2561–2567.
[4] Z. Zeng, N. Stanford, C.H.J. Davies, J.F. Nie, N. Birbilis, Magnesium extrusion alloys: a review of developments and prospects, Int. Mater. Rev. 64 (2019) 27–62.
[5] Y. Wang, H. Choo, Influence of texture on Hall-Petch relationships in an Mg alloy, Acta Mater. 81 (2014) 83–97.
[6] J.A. del Valle, F. Carreño, O.A. Ruano, Influence of texture and grain size on work hardening and ductility in magnesium-based alloys processed by ECAP and rolling, Acta Mater. 54 (2006) 4247–4259.
[7] Z. Zeng, J.F. Nie, S.W. Xu, C.H.J. Davies, N. Birbilis, Super-formable pure magnesium at room temperature, Nat. Commun. 8 (2017) 972.
[8] X. Luo, Z. Feng, T. Yu, J. Luo, T. Huang, G. Wu, N. Hansen, X. Huang, Transitions in mechanical behavior and in deformation mechanisms enhance the strength and ductility of Mg–3Gd, Acta Mater. 183 (2020) 398–407.
[9] Y. Qiao, X. Wang, Z. Liu, E. Wang, Effects of grain size, texture and twinning on mechanical properties and work-hardening behaviors of pure Mg, Mater. Sci. Eng. A 578 (2013) 240–246.
[10] J. Bohlen, M.R. Nürnberg, J.W. Senn, D. Letzig, S.R. Agnew, The texture and anisotropy of magnesium-zinc-rare earth alloy sheets, Acta Mater. 55 (2007) 2101–2112.
[11] R.K. Mishra, A.K. Gupta, P.R. Rao, A.K. Sachdev, A.M. Kumar, A.A. Luo, Influence of cerium on the texture and ductility of magnesium extrusions, Scr. Mater. 59 (2008) 562–565.
[12] Z. Huang, L. Wang, B. Zhou, T. Fischer, S. Yi, X. Zeng, Observation of non-basal slip in Mg-Y by in situ three-dimensional X-ray diffraction, Scr. Mater. 143 (2018) 44–48.
[13] S. Sandlöbes, S. Zaefferer, I. Schestakow, S. Yi, R. Gonzalez-Martinez, On the role of non-basal deformation mechanisms for the ductility of Mg and Mg–Y alloys, Acta Mater. 59 (2011) 429–439.
[14] A. Imandoust, C.D. Barrett, T. Al-Samman, K.A. Inal, H. El Kadiri, A review on the effect of rare-earth elements on texture evolution during processing of magnesium alloys, J. Mater. Sci. 52 (2017) 1–29.
[15] Z. Wu, R. Ahmad, B. Yin, S. Sandlöbes, W.A. Curtin, Mechanistic origin and prediction of enhanced ductility in magnesium alloys, Science 359 (2018) 447–452.

[16] L. Wang, Z. Huang, H. Wang, A. Maldar, S. Yi, J.S. Park, P. Kenesei, E. Lilleodden, X. Zeng, Study of slip activity in a Mg-Y alloy by in situ high energy X-ray diffraction microscopy and elastic viscoplastic self-consistent modeling, Acta Mater. 155 (2018) 138–152.
[17] N. Stanford, R. Cottam, B. Davis, J. Robson, Evaluating the effect of yttrium as a solute strengthener in magnesium using in situ neutron diffraction, Acta Mater. 78 (2014) 1–13.
[18] A. Kula, X. Jia, R.K. Mishra, M. Niewczas, Mechanical Properties of Mg-Gd and Mg–Y Solid Solutions, Metall. Mater. Trans. B 47 (2016) 3333–3342.
[19] J.F. Nie, B.C. Muddle, Characterisation of strengthening precipitate phases in a Mg–Y–Nd alloy, Acta Mater. 48 (2000) 1691–1703.
[20] G. Barucca, R. Ferragut, F. Fiori, D. Lussana, P. Mengucci, F. Moia, G. Riontino, Formation and evolution of the hardening precipitates in a Mg–Y–Nd alloy, Acta Mater. 59 (2011) 4151–4158.
[21] T.T.T. Trang, J.H. Zhang, J.H. Kim, A. Zargaran, J.H. Hwang, B.C. Suh, N.J. Kim, Designing a magnesium alloy with high strength and high formability, Nat. Commun. 9 (2018) 2522.
[22] K.P. Rao, Y.V.R.K. Prasad, C. Dharmendra, K. Suresh, N. Hort, H. Dieringa, Review on Hot Working Behavior and Strength of Calcium-Containing Magnesium Alloys, Adv. Eng. Mater. 20 (2018) 1701102.
[23] E.I. Andritsos, A.T. Paxton, Effects of calcium on planar fault energies in ternary magnesium alloys, Phys. Rev. Mater. 3 (2019) 013607.
[24] S. Sandlöbes, M. Friák, S. Korte-Kerzel, Z. Pei, J. Neugebauer, D. Raabe, A rare-earth free magnesium alloy with improved intrinsic ductility, Sci. Rep. 7 (2017) 10458.
[25] T. Nakata, C. Xu, R. Ajima, K. Shimizu, S. Hanaki, T.T. Sasaki, L. Ma, K. Hono, S. Kamado, Strong and ductile age-hardening Mg–Al–Ca–Mn alloy that can be extruded as fast as aluminum alloys, Acta Mater. 130 (2017) 261–270.
[26] M. Cihova, R. Schäublin, L.B. Hauser, S.S.A. Gerstl, C. Simson, P.J. Uggowitzer, J.F. Löffler, Rational design of a lean magnesium-based alloy with high age-hardening response, Acta Mater. 158 (2018) 214–229.
[27] G. Zhu, L. Wang, H. Zhou, J. Wang, Y. Shen, P. Tu, H. Zhu, W. Liu, P. Jin, X. Zeng, Improving ductility of a Mg alloy via non-basal <a>slip induced by Ca addition, Int. J. Plast. 120 (2019) 164–179.
[28] L. Lutterotti, S. Matthies, H.R. Wenk, MAUD: a friendly Java program for material analysis using diffraction, CPD Newsletter IUCr 21 (1999) 14–15.
[29] S. Tekumalla, S. Seetharaman, N. Quy Bau, W. Leong Eugene Wong, C. Sim Goh, R. Shabadi, M. Gupta, Influence of cerium on the deformation and corrosion of magnesium, J. Eng. Mater. Tech. 138 (2016) 031011.
[30] S. Sankaranarayanan, S. Jayalakshmi, M. Gupta, Effect of nano–Al_2O_3 addition and heat treatment on the microstructure and mechanical properties of Mg–(5.6Ti + 3Al) composite, Mater. Charact. 75 (1970) 150–164.
[31] M.K. Habibi, H. Pouriayevali, A.M.S. Hamouda, M. Gupta, Differentiating the mechanical response of hybridized Mg nano-composites as a function of strain rate, Mater. Sci. Eng. A 545 (2012) 51–60.
[32] N. Stanford, M.R. Barnett, The origin of “rare earth” texture development in extruded Mg-based alloys and its effect on tensile ductility, Mater. Sci. Eng. A 496 (2008) 399–408.
[33] Z.R. Zeng, M.Z. Bian, S.W. Xu, C.H.J. Davies, N. Birbilis, J.F. Nie, Effects of dilute additions of Zn and Ca on ductility of magnesium alloy sheet, Mater. Sci. Eng. A 674 (2016) 459–471.
[34] N. Stanford, M.R. Barnett, Solute strengthening of prismatic slip, basal slip and {10$\bar{1}$2} *twinning in Mg and Mg–Zn binary alloys*, Int. J. Plast. 47 (2013) 165–181.
[35] F. Kabirian, A.S. Khan, T. Gnäupel-Herlod, Visco-plastic modeling of mechanical responses and texture evolution in extruded AZ31 magnesium alloy for various loading conditions, Int. J. Plast. 68 (2015) 1–20.
[36] H.Y. Wang, E.S. Xue, X.L. Nan, T. Yue, Y.P. Wang, Q.C. Jiang, Influence of grain size on strain rate sensitivity in rolled Mg-3Al-3Sn alloy at room temperature, Scripta Mater. 68 (2013) 229–232.
[37] Y.Z. Du, X.G. Qiao, M.Y. Zheng, D.B. Wang, K. Wu, I.S. Golovin, Effect of microalloying with Ca on the microstructure and mechanical properties of Mg–6 mass%Zn alloys, Mater. Des. 98 (2016) 285–293.
[38] B. Lv, J. Peng, Y. Peng, A. Tang, The effect of addition of Nd and Ce on the microstructure and mechanical properties of ZM21 Mg alloy, J. Mag. Alloys 1 (2013) 94–100.
[39] T. Nakata, C. Xu, R. Ajima, Y. Matsumoto, K. Shimizu, T.T. Sasaki, K. Hono, S. Kamado, Improving mechanical properties and yield asymmetry in high-speed extrudable Mg–1.1Al–0.24Ca (wt%) alloy by high Mn addition, Mater. Sci. Eng. A 712 (2018) 12–19.
[40] R.K. Sabat, A.P. Brahme, R.K. Mishra, K. Inal, S. Suwas, Ductility enhancement in Mg–0.2%Ce alloys, Acta Mater. 161 (2018) 246–257.
[41] H. Somekawa, D.A. Basha, A. Singh, Role of grain boundaries on ductility in Mg–Y alloys, Materialia 8 (2019) 100466.
[42] J. Wang, L. Wang, G. Zhu, B. Zhou, T. Ying, X. Zhang, Q. Huang, Y. Shen, X. Zeng, H. Jiang, Understanding the high strength and good ductility in LPSO-containing Mg alloy using synchrotron X-ray diffraction, Metall. Mater. Trans. A 49 (2018) 5382–5392.
[43] P. Hidalgo-Manrique, J.D. Robson, M.T. Pérez-Prado, Precipitation strengthening and reversed yield stress asymmetry in Mg alloys containing rare-earth elements: a quantitative study, Acta Mater. 124 (2017) 456–467.
[44] M. Lentz, M. Klaus, M. Wagner, C. Fahrenson, I.J. Beyerlein, M. Zecevic, W. Reimers, M. Knezevic, Effect of age hardening on the deformation behavior of an Mg–Y–Nd alloy: in-situ X-ray diffraction and crystal plasticity modeling, Mater. Sci. Eng. A 628 (2015) 396–409.
[45] W.Y. Yu, N. Wang, X.B. Xiao, B.Y. Tang, L.M. Peng, W.J. Ding, First-principles investigation of the binary AB2 type Laves phase in Mg–Al–Ca alloy: electronic structure and elastic properties, Solid State Sci. 11 (2009) 1400–1407.
[46] X. Zhang, M. Li, J.-.S. Park, P. Kenesei, J. Almer, C. Xu, J.F. Stubbins, In situ high-energy X-ray diffraction study of tensile deformation of neutron-irradiated polycrystalline Fe-9%Cr alloy, Acta Mater 126 (2017) 67–76.
[47] M. Zhang, R.G. Li, J. Ding, H.Y. Chen, J.-.S. Park, J. Almer, Y.D. Wang, In situ high-energy X-ray diffraction mapping of Lüders band propagation in medium-Mn transformation-induced plasticity steels, Mater. Res. Lett. 6 (2018) 662–667.
[48] Z.W. Zhu, C.Y. Xiong, J. Wang, R.G. Li, Y. Ren, Y.D. Wang, Y. Li, In situ synchrotron X-ray diffraction investigations of the physical mechanism of ultra-low strain hardening in Ti-30Zr-10Nb alloy, Acta Mater. 154 (2018) 45–55.
[49] B. Zhou, L. Wang, G. Zhu, J. Wang, W. Wen, X. Zeng, Understanding the strengthening effect of β_1 precipitates in Mg–Nd Using in situ synchrotron X-ray diffraction, JOM 70 (2018) 2315–2320.
[50] M.F. Ashby, John Wiley & Sons, New York, NY, 1971, pp. 137–192.
[51] H. Yu, C. Li, Y. Xin, A. Chapuis, X. Huang, Q. Liu, The mechanism for the high dependence of the Hall-Petch slope for twinning/slip on texture in Mg alloys, Acta Mater. 128 (2017) 313–326.
[52] H. Mecking, U.F. Kocks, Kinetics of flow and strain-hardening, Acta Metall. 29 (1981) 1865–1875.
[53] L.M. Cheng, W.J. Poole, J.D. Embury, D.J. Lloyd, The influence of precipitation on the work-hardening behavior of the aluminum alloys AA6111 and AA7030, Metall. Mater. Trans. A 34 (2003) 2473–2481.
[54] E. Deligoz, K. Colakoglu, H. Ozisik, Y.O. Cifti, The first principles investigation of lattice dynamical and thermodynamical properties of Al_2Ca and Al_2Mg compounds in the cubic Laves structure, Comp. Mater. Sci. 68 (2013) 27–31.
[55] Z. Wu, W.A. Curtin, The origins of high hardening and low ductility in magnesium, Nature 526 (2015) 62–67.
[56] R. Ahmad, B. Yin, Z. Wu, W.A. Curtin, Designing high ductility in magnesium alloys, Acta Mater. 172 (2019) 161–184.
[57] B.Y. Liu, N. Yang, J. Wang, M. Barnett, Y.C. Xin, D. Wu, R.L. Xin, B. Li, R.L. Narayan, J.F. Nie, J. Li, E. Ma, Z.W. Shan, Insight from in situ microscopy into which precipitate morphology can enable high strength in magnesium alloys, J. Mater. Sci. Technol. 34 (2018) 1061–1066.
[58] B.Y. Liu, F. Liu, N. Yang, X.B. Zhai, L. Zhang, Y. Yang, B. Li, J. Li, E. Ma, J.F. Nie, Z.W. Shan, Large plasticity in magnesium mediated by pyramidal dislocations, Science 365 (2019) 73–75.
[59] H. Pan, R. Kang, J. Li, H. Xie, Z. Zeng, Q. Huang, C. Yang, Y. Ren, G. Qin, Mechanistic investigation of a low-alloy Mg–Ca-based extrusion alloy with high strength-ductility synergy, Acta Mater. 186 (2020) 278–290.
[60] Z.R. Zeng, Y.M. Zhu, S.W. Xu, M.Z. Bian, C.H.J. Davies, N. Birbilis, J.F. Nie, Texture evolution during static recrystallization of cold-rolled magnesium alloys, Acta Mater. 105 (2016) 479–494.
[61] T. Tsuru, H. Somekawa, D.C. Chrzan, Interfacial segregation and fracture in Mg-based binary alloys: experimental and first-principles perspective, Acta Mater. 151 (2018) 78–86.
[62] H. Somekawa, D.A. Basha, A. Singh, T. Tsuru, M. Yamaguchi, Non-basal dislocation nucleation site of solid solution magnesium alloy, Mater. Trans. 61 (2020) 1172–1175.